

## Optimization of penetration depth and powder layer thickness for proper interlayer adhesion in polymer laser sintering

Yuki Yamauchi\*†, Takashi Kigure\*, and Toshiki Niino†

\*Tokyo Metropolitan Industrial Technology Research Institute, Aomi, Koto-ku, Tokyo,  
135-0064

†Institute of Industrial Science, the University of Tokyo, Komaba, Meguro-ku, Tokyo,  
153-8505

### Abstract

In laser sintering, the melt pool depth relative to the powder layer thickness is the main factor influencing interlayer adhesion strength. The melt pool depth is closely related to the amount of laser energy and its penetration depth. Previous studies have shown that using a near-infrared laser and an additive agent that absorbs its light allows for a wide range of penetration depth control. This research focuses on the optimization of the powder layer thickness and penetration depth to achieve appropriate interlayer adhesion. To determine the optimal amount of laser energy, the relationship between the amount of laser energy and part density for each layer pitch and penetration depth was determined. The relationship between the amount of energy supplied normalized by the penetration depth and part density was consistent regardless of the penetration depth of the powder material. The adhesion strength of specimens prepared using different optimal amounts of energy to maximize part density was evaluated. Based on this evaluation, layer thickness normalized by penetration depth is the dominant factor influencing interlayer adhesion strength.

### Introduction

Additive manufacturing is expected to produce not only prototypes but also end-use parts. Laser sintering, which can be used for high-performance materials as well as injection molding, is one of the most promising technologies. In the laser sintering process, parts are fabricated in such a way that the powder materials used are fused with laser irradiation layer by layer, and the fused resin is bonded to the previously processed layers[1]. The bonding quality of each layer directly affects the quality of the part built, such as mechanical properties. To optimize interlayer bonding, an in-depth understanding of the heating, melting, and bonding processes of powder materials is required. In particular, the major factors determining interlayer adhesion strength are the thickness of the powder layer and the melt pool depth in each layer. If the melt pool is shallower than the thickness of the powder layer, the layers do not adhere. The melt pool depth depends on the amount of laser energy supplied and the depth to which that energy reaches the powder material. The relationship between energy supplied and part quality, including adhesion strength, has already been investigated[2][3][4], and the laser energy supplied is typically adjusted when determining laser sintering conditions. However, because the optimal energy supplied varies depending on powder material,

filler, and the amount added, it must be adjusted individually. To provide a more systematic index for the optimization of energy supplied, Starr et al. introduced the energy melt ratio (EMR), which is the ratio of laser energy to the amount of energy required to melt the powder layer[5][6]. The EMR can be used to evaluate energy supplied using uniform parameters, even for different materials.

On the other hand, the relationship between the depth at which a laser incident on a powder layer reaches, referred to as the penetration depth in Figure 1, and interlayer adhesion strength has not been studied. The penetration depth is a unique optical parameter determined by both the powder material and laser wavelength. Most commercially available systems are equipped with a long-wavelength CO<sub>2</sub> laser with high resin absorption as the light source, which means that most of the laser energy does not penetrate the powder layer[7][8]. Although Fan et al. attempted to adjust the penetration depth of CO<sub>2</sub> lasers by adding transparent additives, it could not be changed significantly[9]. In contrast, a method has been proposed that uses a near-infrared laser rarely absorbed by most polymeric materials and adds an absorbing agent, allowing for a wide range of penetration depth adjustment[10][11]. In addition, the penetration depth is positively correlated with the melt pool depth[12]. To better understand the relationship between the penetration depth and interlayer adhesion strength, further investigation is required.

This study focused on optimizing the amount of laser energy supplied and the penetration depth for various powder layer thicknesses to obtain the appropriate interlayer adhesion strength. First, the optimal amount of laser energy supplied for each powder layer thickness was determined on the basis of the built part density using powder materials with various penetration depths. Next, specimens were fabricated using the optimized laser energy, and the interlayer adhesion strength was evaluated. Finally, the optimal penetration depth was discussed on the basis of the relationship between adhesion strength and layer thickness normalized by the penetration depth.

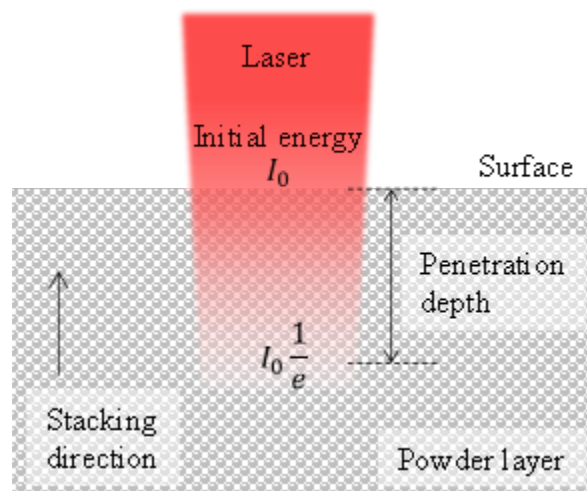


Figure 1 Schematic image of laser penetrating powder layer. Penetration depth is the depth at which the initial energy attenuates to 1/e, assuming that the attenuation of laser energy incident on the powder layer follows Beer–Lamber's law.

## **Material and Methods**

### Penetration depth of powder material

The polymer powder used was PA12 (VESTOSINT X1556, POLYPLASTICS EVONIK, Japan). This powder has an average particle size of 55  $\mu\text{m}$ , a true density of 1.03  $\text{g}/\text{cm}^3$ , a melting point of 182°C, and a recrystallization temperature of 144°C. A resin dye (NUBIAN BLACK PC-0870, ORIENT CHEMICAL INDUSTRIES, Japan) was used as the absorbing agent. The absorbent has an average particle diameter of 10  $\mu\text{m}$  and a true density of 1.24  $\text{g}/\text{cm}^3$ . The powder and absorbent were mixed for 1 hour using a mixer (SKH-100, MISUGI, Japan). The relationship between absorbent content and penetration depth of near-infrared light (a wavelength of 1  $\mu\text{m}$ ) for these materials has already been reported by the authors[12].

### Specimen preparation and density measurement

Specimens for density evaluation were in the form of 10 × 10 × 5-mm blocks. The specimens were fabricated using a commercially available laser sintering machine (RaFaEl 300F, Aspect, Japan) equipped with a 1- $\mu\text{m}$  near-infrared laser. The processing conditions for the specimens are presented in Table 1. The amount of energy supplied, known as the energy density in the table is expressed using the following equation

$$E_a = \frac{P}{vs}, \quad (1)$$

where  $P$ ,  $v$ , and  $s$  denote laser power, laser scanning speed, and scan spacing in raster scanning. The laser scan is fixed to the same x-axis as the direction of operation of a recoater in all layers, with no so-called "cross-hatching". "Layer pitch" in the table 1 refers to the amount of descent of the machine platform at each layer. It is commonly known as "layer thickness," but this paper makes a clear distinction for the reasons described below.

Table 1 Processing parameters of block-shaped specimens for density measurement

Parameter	Setpoint				
Absorbent content [wt%] (Penetration depth $\mu\text{m}$ )	0.1 (378)	0.2 (275)	0.6 (167)	1.0 (130)	1.8 (97)
Bed Temperature [ $^{\circ}\text{C}$ ]	30				
Layer pitch [ $\mu\text{m}$ ]	50-150				
Beam diameter [ $\mu\text{m}$ ]	150				
Scan Speed [m/s]	0.5				
Scan interval [mm]	0.05				
Laser powder [W]	15-50	8-34	5-20	4-16	2-14
Energy density [ $\text{kJ}/\text{m}^2$ ]	600-2000	320-1360	200-800	160-640	80-560

The powder bed was not preheated to build under the same condition as during the penetration depth measurement. When laser sintering at room-temperature powder beds, the stacking process is halted because the molten resin solidifies and shrinks immediately after the laser irradiation is stopped, causing warpage. To suppress this warpage, a low-temperature process, which has been previously proposed by the authors, was used[13][14]. In this low-temperature process, a rigid base plate is placed on the platform of the laser sintering machine, and parts and the base plate are bound together by a sacrificial structure built through the same process. The apparent density of the built specimen was obtained following the Archimedes principle using a hydrometer (AUX-220, SHIMADZU, Japan). On the basis of the ratio of apparent density to true density, a relative density was obtained. In this study, the absorbent content was not considered when calculating the relative density because the absorbent content is at most 2% or less and could be vaporized by intensive heating due to laser irradiation.

#### Microstructure observation

To understand the melting process, a cross-sectional image of the part was observed using a microscope (KH-8700, HIROX, Japan). Thin sections for microscopic observation with transmitted light were prepared using a microtome (RV-240N, YAMATO KOHKI INDUSTRIAL, Japan). The thin sections were obtained from the yz plane across the center of the specimen.

#### Tensile test

The tensile strength in the stacking direction of the specimens, which is directly related to the adhesion strength between the layers[15], was evaluated. The geometry of the specimens was half size, as described in ISO 527. The longitudinal direction of the specimens was placed in the z-axis direction (the stacking direction) as shown in

Figure 2. The processing parameters of the specimens are presented in Table 2. The same values as in Table 1 were used for bed temperature, scanning speed, and scanning interval. The energy densities in the table were optimized to maximize the density of the block-shaped specimens. To reduce the effects of the surface properties of the specimens on the adhesion strength, the specimens were polished with an abrasive paper before the tensile test. Tensile tests were conducted using a universal testing system (INSTRON 3366, 10 kN load cell, Instron, USA) following ISO 527. Young's modulus was determined using an extensometer (2630-120, Instron, USA) and analysis software (Bluehill, Instron, USA) within the 0.05%–0.25% strain range. Elongation at break (EaB) was determined by the displacement of the crosshead. The travel speed of the crosshead was 0.5 mm/min up to 0.25% strain and 2 mm/min thereafter.

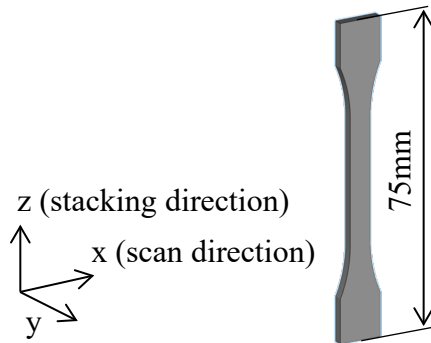


Figure 2 Build orientation of tensile specimen  
Table 2 Processing parameters of specimens for tensile test

Absorbent content [wt%] (Penetration depth $\mu\text{m}$ )	Layer pitch [ $\mu\text{m}$ ]	Laser power [W]	Energy density [kJ/m <sup>2</sup> ]
0.1 (378)	50	27.0	1080
	75	31.0	1240
	100	33.0	1320
	125	35.0	1400
	150	36.0	1440
0.2 (275)	50	21.0	840
	75	23.0	920
	100	23.0	920
	125	25.0	1000
	150	26.0	1040
0.6 (167)	50	10.5	420
	75	10.5	420
	100	11.5	460
	125	11.5	460
	150	11.5	460
1.0 (130)	50	7.0	280
	75	8.0	320
	100	9.0	360
	125	9.0	360
	150	9.0	360
1.8 (97)	50	5.0	200
	75	5.5	220
	100	6.0	240
	125	6.0	240
	150	6.5	260

## Results

### Part density

The relationship between the energy density and relative density of the specimens is shown in Figures 3 and 4. Note that the results for a layer pitch of 100  $\mu\text{m}$  are included in the authors' previous paper[12]. For all penetration depths, the relative density tends to increase as the energy density increases. For small penetration depths, the relative density decreases rapidly above a certain energy density. An increase in penetration depth necessitates an increase in energy density, increasing the relative density. These trends are similar for layer pitches of 100 and 150  $\mu\text{m}$  as well. On the other hand, when the energy density remains constant, the relative density decreases, and the energy required to maximize the density increases as the layer pitch increases.

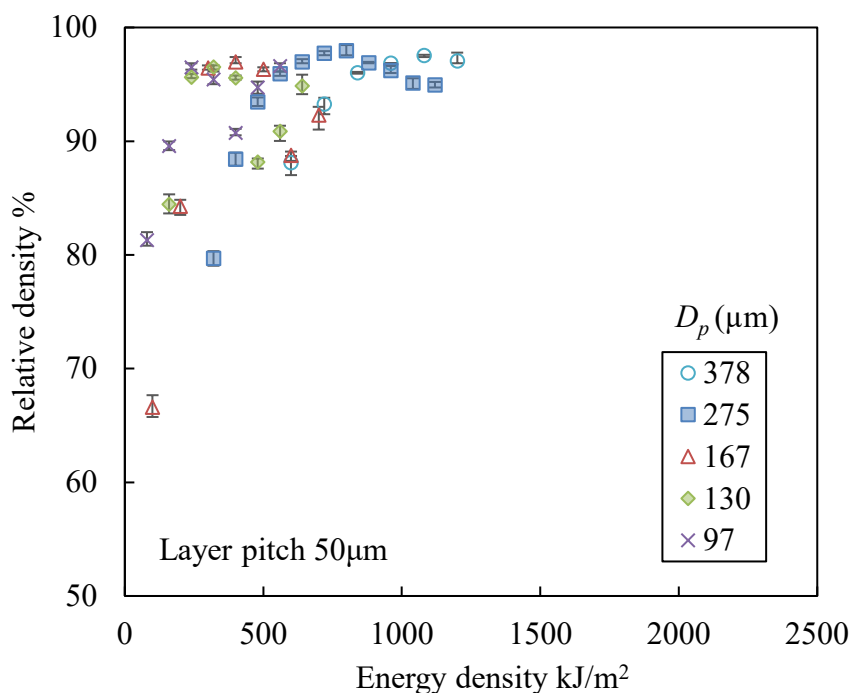


Figure 3 Relative density for each penetration depth in a layer pitch of 50  $\mu\text{m}$ . The error bars represent the maximum and minimum values out of a sample number of 5.  $D_p$  in the graph represents the penetration depth.

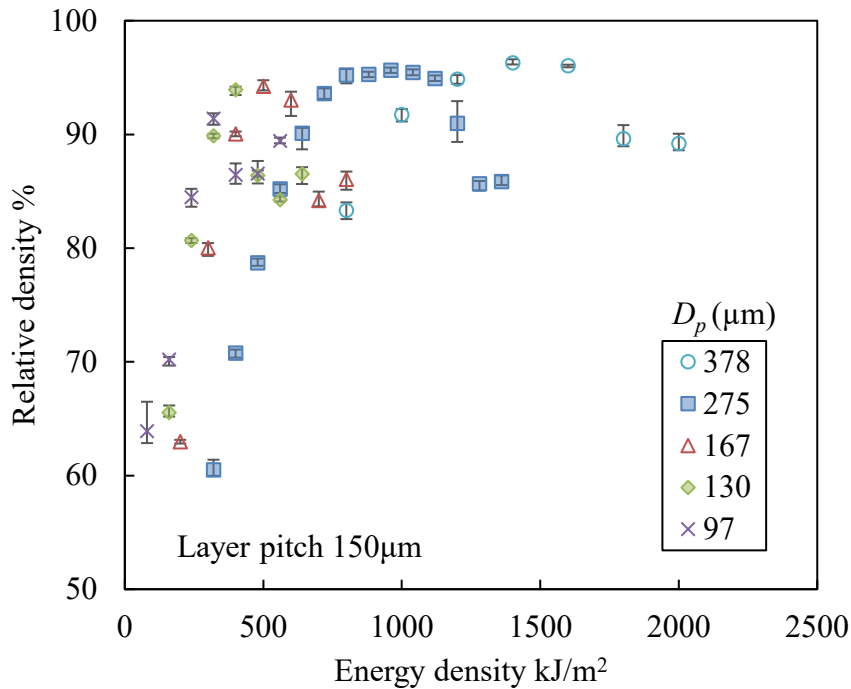
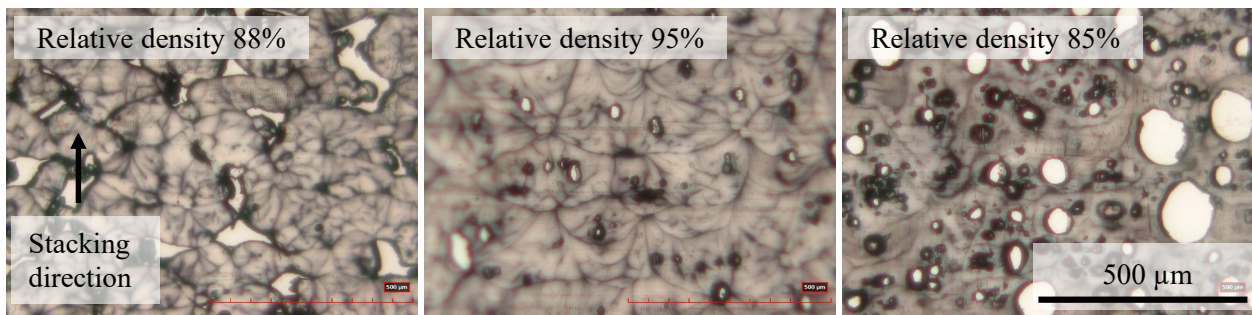


Figure 4 Relative density for each penetration depth in a layer pitch of 150 μm

#### Microstructure observation

Figure 5 depicts a cross-sectional image of a part built under a penetration depth of 130 μm and a layer pitch of 100 μm. Here, the energy at which the maximum density is obtained under each condition is defined as  $E_{a\ max}$  (a) is the cross-section of a specimen when  $<E_{a\ max}$ , (b) when  $E_{a\ max}$ , and (c) when  $>E_{a\ max}$ , and the relative densities of each specimen were 88, 95, and 85%, respectively. Compared to (a) and (b), large spherical voids can be observed in the cross-section of (c).



a)  $D_p$  130 μm,  $E_a$  = 240 kJ/m<sup>2</sup>

b)  $D_p$  130 μm,  $E_a$  = 400 kJ/m<sup>2</sup>

c)  $D_p$  130 μm,  $E_a$  = 480 kJ/m<sup>2</sup>

Figure 5 Transmission micrograph of built specimens; a) relative density not reached the top; b) relative density reached maximum; c) relative density decrease occurred. Bright areas represent voids, black parts are absorbent agents, and others are resins.

## Tensile test

Figure 6 depicts the relationship between layer pitch and ultimate tensile strength (UTS) in the z-axis direction. For all penetration depths, UTS tended to decrease as the layer pitch increased. For penetration depths less than 167  $\mu\text{m}$ , UTS decreased with decreasing penetration depth and the slope of the decrease appeared to be the same. For a penetration depth of 378  $\mu\text{m}$ , UTS for the layer pitch of between 50 and 100  $\mu\text{m}$  remains almost the same.

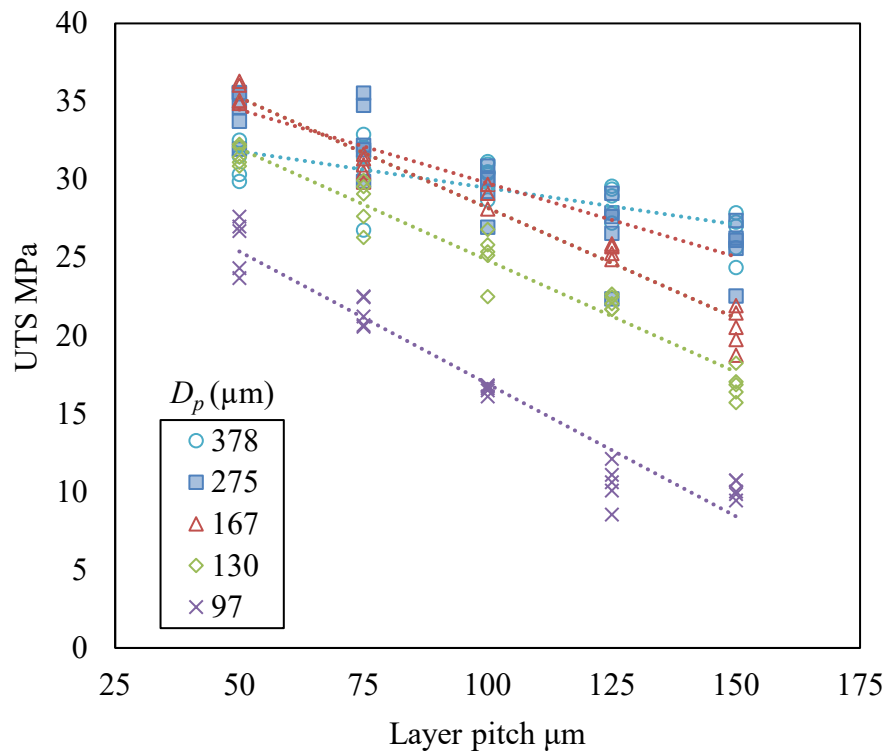


Figure 6 Relationship between layer pitch and UTS for each penetration depth. The dotted lines indicate approximate straight lines.

Figure 7 depicts the relationship between layer pitch and Young's modulus in the z-axis direction, which, similar to UTS, shows a downward trend, but the slope of the decrease becomes shallower as the penetration depth increases.

As shown in Figure 8, the EaB in the z-axis direction tends to decrease as the layer pitch increases. The slope also decreases with increasing penetration depth. Unlike the other result, relatively high EaB values were obtained at penetration depths of 167 and 275  $\mu\text{m}$ .

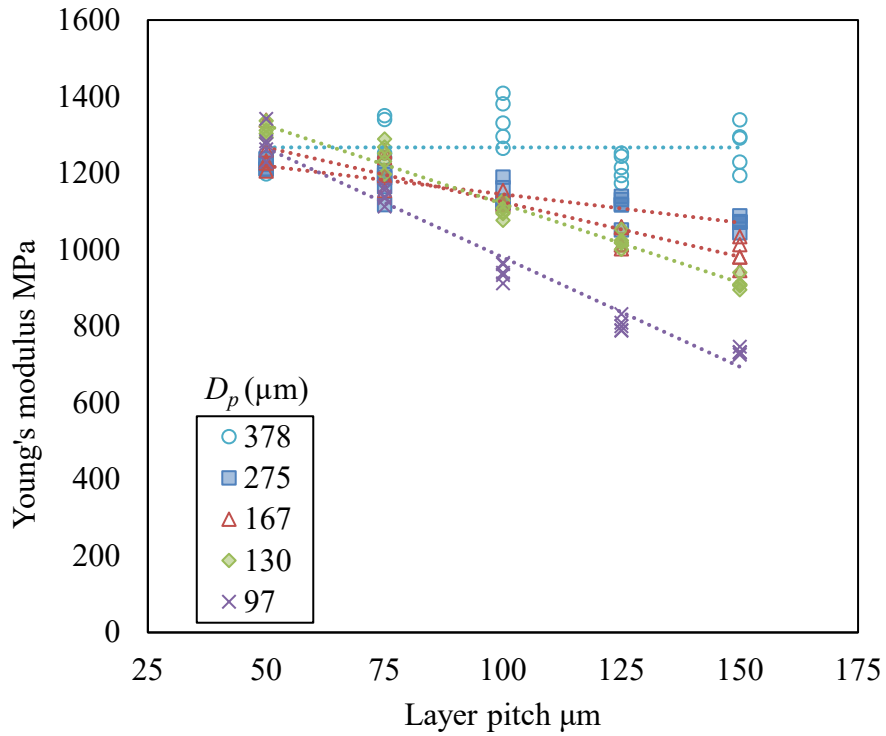


Figure 7 Relationship between layer pitch and Young's modulus for each penetration depth.

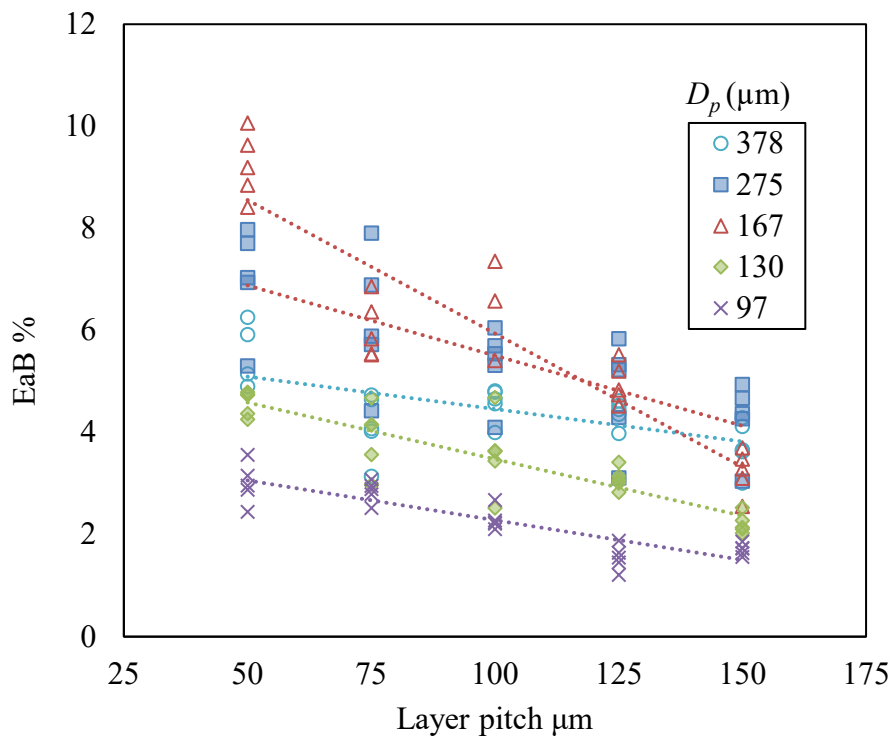


Figure 8 Relationship between layer pitch and EaB for each penetration depth.

## Discussion

### Laser energy optimization

The relative density of a built part increases as the powder melts and molten resin fills the voids in the powder layer. The molten resin flows more easily at higher temperatures in this process. The temperature of the molten resin varies with the amount of laser energy absorbed by the powder. However, the energy density in Equation 1 does not consider optical phenomena such as transmission and absorption of laser incident on the powder bed. When the penetration depth is large, indicating low absorption, more laser energy is required to melt the powder. In other words, each time materials or fillers that affect optical properties are changed, the energy density must be optimized according to experiments. Here, we introduce an energy density normalized by the penetration depth, as shown in Equation 2, to consider optical properties.

$$E_{nv} = \frac{E_a}{D_p}, \quad (2)$$

where  $D_p$  represents the penetration depth. Assuming that all energy is absorbed by the powder material until laser light reaches the penetration depth,  $E_{nv}$  is equivalent to the amount of energy supplied per unit volume. Figures 9, 10, and 11 show the relationship between  $E_{nv}$  and relative density of the built specimen for the layer pitch of 50, 100, and 150  $\mu\text{m}$ . For  $E_{nv}$  less than 3.5  $\text{MJ}/\text{mm}^3$ , the relationship between  $E_{nv}$  and relative density in each layer pitch was consistent for all penetration depths, and the maximum relative density is obtained when  $E_{nv}$  is around 3.0  $\text{MJ}/\text{mm}^3$ . Thus, the optimal  $E_{nv}$  is 3.0  $\text{MJ}/\text{mm}^3$  in this study.

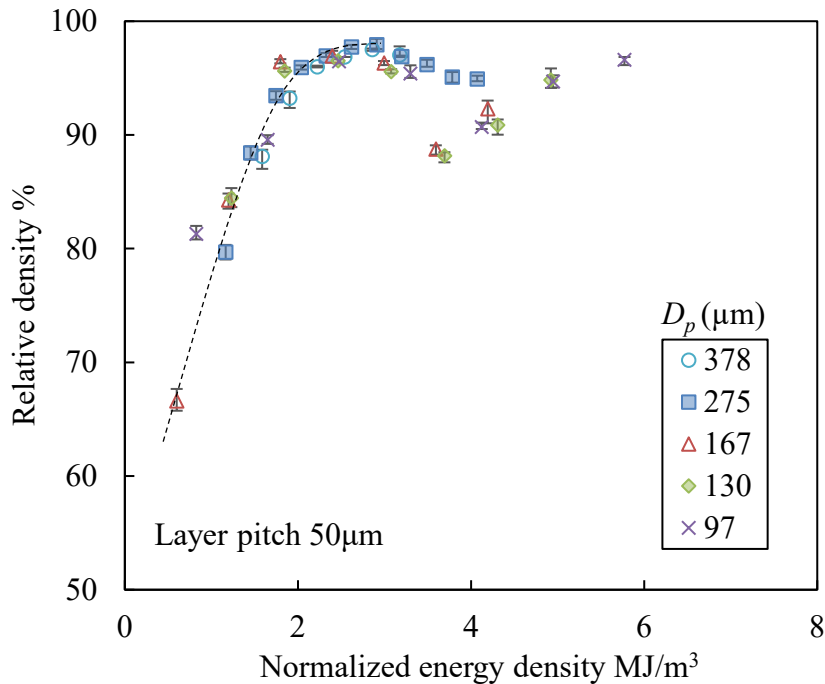


Figure 9 Relationship between  $E_{nv}$  and relative density for a layer pitch of 50  $\mu\text{m}$ .

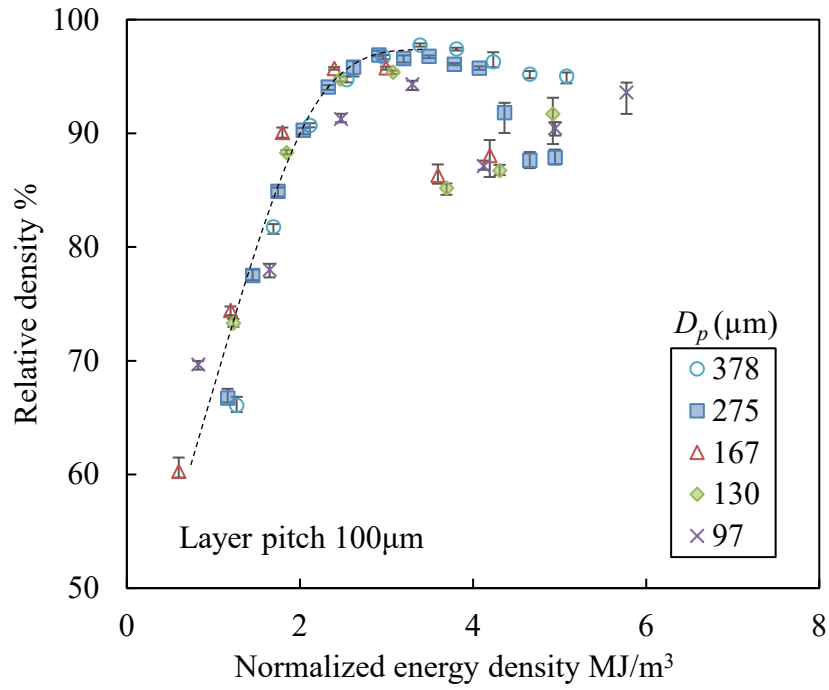


Figure 10 Relationship between  $E_{nv}$  and relative density for a layer pitch of 100  $\mu\text{m}$ .

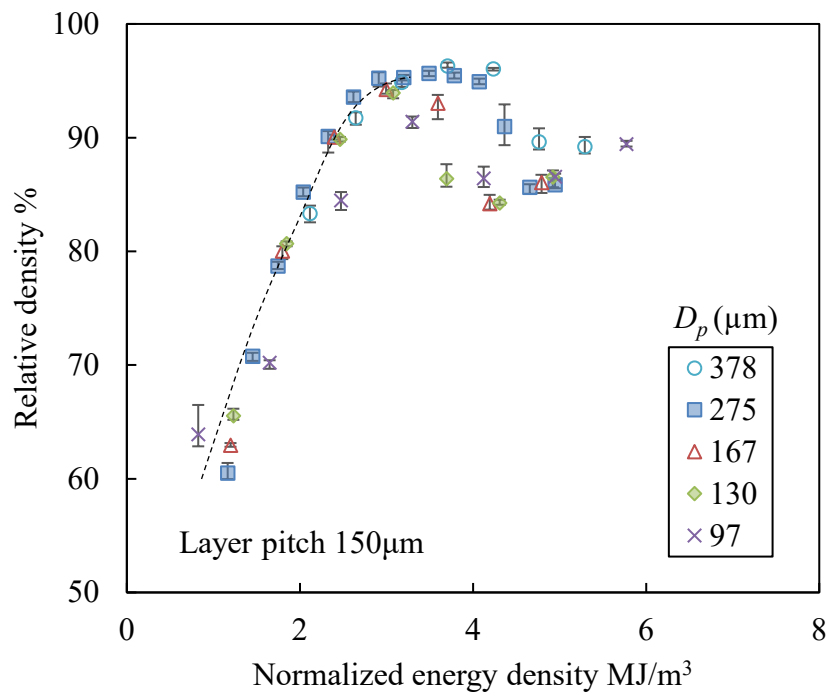


Figure 11 Relationship between  $E_{nv}$  and relative density for a layer pitch of 150  $\mu\text{m}$ .

The above discussion suggests that we can control the melt resin temperature and part density with  $E_{nv}$  even if optical properties change, as long as they are known. However, for small penetration depths, the part density decreases dramatically when  $E_{nv}$  exceeds 3.5 MJ/mm<sup>3</sup> in any layer pitch. A small penetration depth means that a significant amount of energy is absorbed intensively near the surface. As a result, it is assumed that the molten resin temperature near the surface is higher than the decomposition temperature[16]. According to Vasquez et al., the decomposition temperature of PA12 powder is 320°C–360°C[6]. Unlike the other specimen, relatively large spherical voids were also observed in the cross-sectional images of the specimens in which density reduction occurred (Figure 5 (c)), supporting the above assumption.

### Optimization of normalized powder layer thickness

The influence of penetration depth on interlayer adhesion strength is discussed. As mentioned in the introduction section, the melt pool depth must be larger than the layer pitch for layer adhesion and to improve adhesion strength. Past research results by the authors have shown that the melt pool depth is positively correlated with the penetration depth. Therefore, the penetration depth relative to the powder layer thickness has a strong influence on the adhesion strength. Here, we normalize the layer thickness by the penetration depth and discuss the optimal layer thickness to obtain the appropriate adhesion strength. Note that the powder layer thickness and layer pitch are not equated in the bonding area. More than half of the volume of the PA12 powder used in this study is air voids. As the powder material melts during processing and air is removed, the surface position of the processed area is lowered[17][18][19]. When the platform is lowered by the layer pitch, a powder layer thicker than the pitch is formed in the next layer. By a simple calculation, powder layer thickness in the bonding area  $\ell_{lt}$  is calculated using Equation 3.

$$\ell_{lt} = \frac{\rho_s}{\rho_p} \ell_{lp}, \quad (3)$$

where  $\rho_p$ ,  $\rho_s$ , and  $\ell_{lp}$  represent the apparent density of the powder layer, the apparent density of the processing region which is equivalent to the relative density of built part, and the layer pitch, respectively. Normalizing the powder layer thickness by the penetration depth is given by Equation 4.

$$\ell_{nlt} = \frac{\ell_{lt}}{D_p} \quad (4)$$

As shown in Figure 12, the relationship between  $\ell_{nlt}$  and UTS is almost the same regardless of the absorbent content with a flat or gradual decreasing trend in UTS up to a  $\ell_{nlt}$  of 0.7 and an obvious downward trend above 0.7. From this relationship,  $\ell_{nlt}$  for proper interlayer adhesion is 0.7 or less. Young's modulus also shows a trend similar to that of UTS, as shown in Figure 13, with smaller changes for  $\ell_{nlt} < 1$ . In addition, as shown in Figure 14, the largest value of elongation with  $\ell_{nlt} < 0.7$  is obtained at a penetration depth of 167  $\mu\text{m}$ . Therefore, the optimal penetration depth and powder layer thickness in this study are 167 and 110  $\mu\text{m}$ , respectively. However, the relationship between the penetration depth and elongation in the stacking direction remains unclear and requires further investigation.

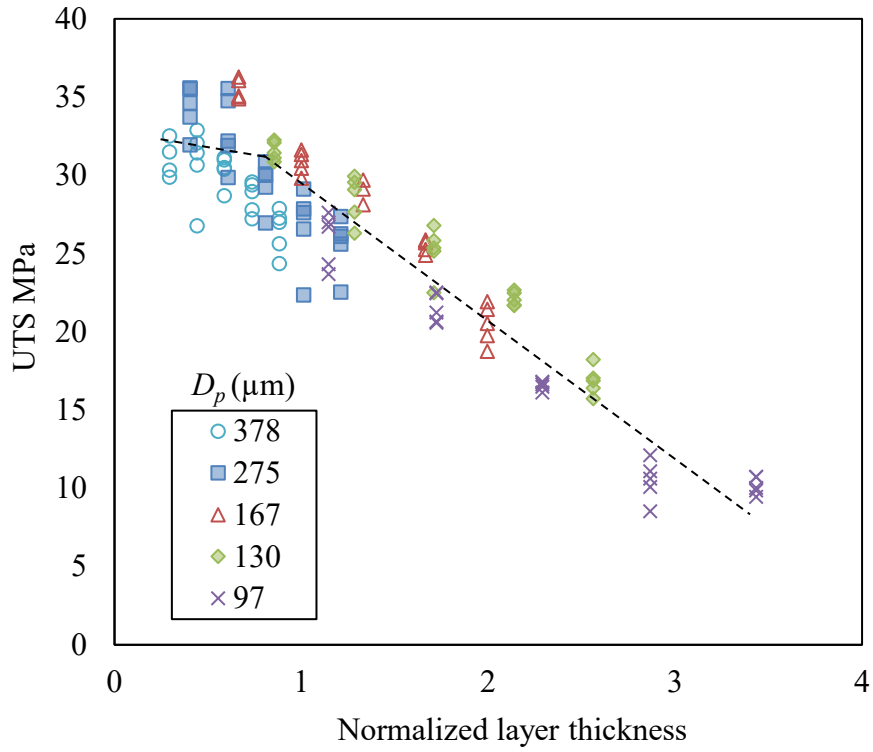


Figure 12 Relationship between  $\ell_{nlt}$  and UTS.

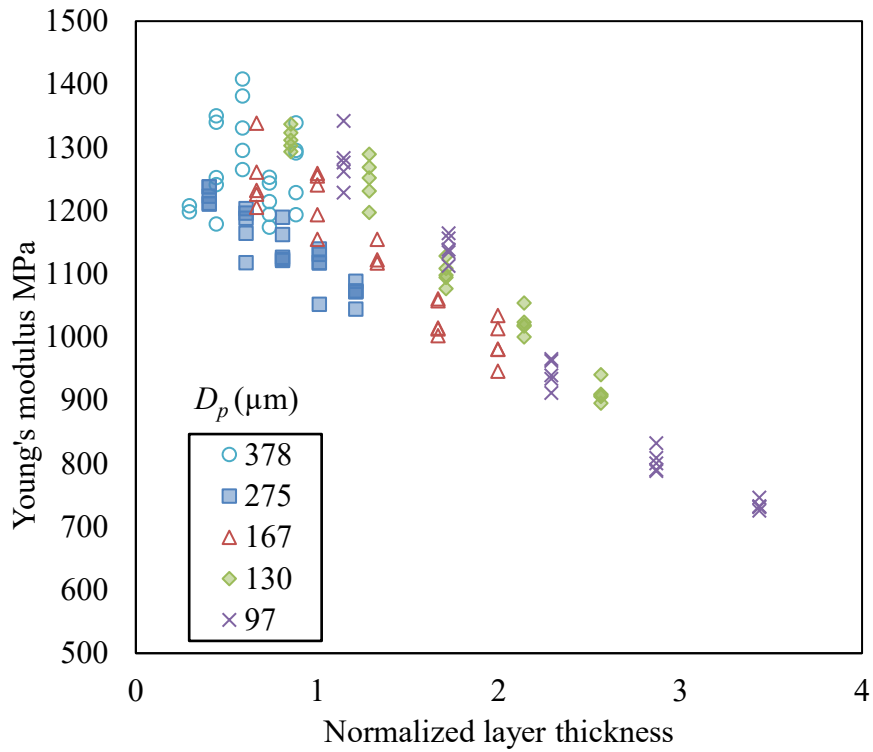


Figure 13 Relationship between  $\ell_{nlt}$  and Young's modulus.

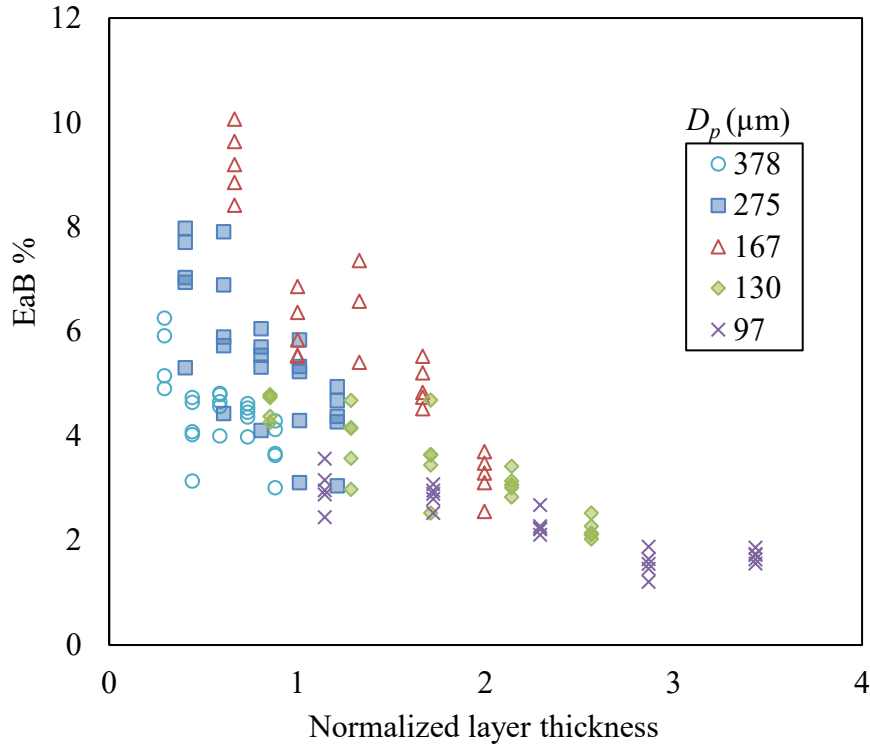


Figure 14 Relationship between  $\ell_{nlt}$  and EaB.

### **Conclusion**

In this study, to understand the role of the amount of laser energy supplied and its depth on powder melting and interlayer bonding, the following investigations were performed. First, a relationship between the amount of energy supplied and built part density was obtained for each layer thickness and penetration depth. The results show that larger penetration depths require more laser energy to increase the part density. In contrast, the relationship between energy supplied normalized by the penetration depth and part density is consistent regardless of the penetration depth. Based on the results, the amount of energy supplied at each penetration depth and layer pitch was optimized to maximize the part density. Next, mechanical properties in the stacking direction of parts built using the optimal amount of laser energy supplied were evaluated, and the relationship between penetration depth and interlayer adhesion strength was discussed. The results show that there is a strong correlation between the powder layer thickness normalized by the penetration depth and UTS, which is closely related to adhesion strength. In addition, the optimal penetration depth and powder layer thickness to ensure appropriate adhesion strength between layers are presented. These findings suggest that optimal processing conditions can be determined more systematically by understanding optical properties such as the penetration depth of laser light incident on powder layers.

### **Acknowledgment**

This research was partially supported by the Ministry of Education, Science, Sports and Culture, Grant-in-Aid for Early-Career Scientists, 2020–2023 (20K14634, Yuki Yamauchi) .

## References

- [1] D.K. Leigh, A comparison of polyamide 11 mechanical properties between laser sintering and traditional molding, 23rd Annu. Int. Solid Free. Fabr. Symp. - An Addit. Manuf. Conf. SFF 2012. (2012) 574–605.
- [2] A. Pilipovic, B. Valentan, T. Brajljih, T. Haramina, J. Balic, J. Kodvanj, M. Sercer, I. Drstvensek, Influence of laser sintering parameters on mechanical properties of polymer products, Ann. DAAAM Proc. Int. DAAAM Symp. (2010) 285–286.
- [3] Y. Khalil, A. Kowalski, N. Hopkinson, Influence of energy density on flexural properties of laser-sintered UHMWPE, Addit. Manuf. 10 (2016) 67–75. <https://doi.org/10.1016/j.addma.2016.03.002>.
- [4] M. Pavan, M. Faes, D. Strobbe, B. Van Hooreweder, T. Craeghs, D. Moens, W. Dewulf, On the influence of inter-layer time and energy density on selected critical-to-quality properties of PA12 parts produced via laser sintering, Polym. Test. 61 (2017) 386–395. <https://doi.org/10.1016/j.polymertesting.2017.05.027>.
- [5] T.L. Starr, T.J. Gornet, J.S. Usher, The effect of process conditions on mechanical properties of laser-sintered nylon, Rapid Prototyp. J. 17 (2011) 418–423. <https://doi.org/10.1108/13552541111184143>.
- [6] M. Vasquez, B. Haworth, N. Hopkinson, Methods for Quantifying the Stable Sintering Region in Laser Sintered Polyamide-12, Polym. Eng. Sci. 53 (2012) 1230–1240. <https://doi.org/10.1002/pen>.
- [7] T. Laumer, K. Wudy, M. Drexler, P. Amend, S. Roth, D. Drummer, M. Schmidt, Fundamental investigation of laser beam melting of polymers for additive manufacture, J. Laser Appl. 26 (2014) 042003. <https://doi.org/10.2351/1.4892848>.
- [8] B. Keller, R. Pfeifer, W.N. Su, P. Eyerer, Temperature dependent optical properties of polymers as a basis for laser process modelling, Solid Free. Fabr. Proc. (1998) S. 549-556.
- [9] K.M. Fan, K.W. Wong, W.L. Cheung, I. Gibson, Reflectance and transmittance of TrueForm™ powder and its composites to CO2 laser, Rapid Prototyp. J. 13 (2007) 175–181. <https://doi.org/10.1108/13552540710750924>.
- [10] A.P. John A. Benda, Absorption tailored laser sintering, (1998).
- [11] M. Kroh, P. Eyerer, ADDITIVE ASSISTED LASER SINTERING OF POLYETHERETHERKETONE, Stuttgarter Kunststoff-Kolloquium. (2009) 1–8.
- [12] Y. Yamauchi, T. Kigure, K. Isoda, T. Niino, Powder bed penetration depth control in laser sintering and effect on depth of fusion, Addit. Manuf. 46 (2021) 102219. <https://doi.org/10.1016/j.addma.2021.102219>.
- [13] T. Niino, H. Haraguchi, Y. Itagaki, S. Iguchi, M. Hagiwara, Feasibility study on plastic laser sintering without powder bed preheating, 22nd Annu. Int. Solid Free. Fabr. Symp. - An Addit. Manuf. Conf. SFF 2011. (2011) 17–29.
- [14] Y. Yamauchi, T. Kigure, T. Niino, Low temperature laser sintering of PA powder using fiber laser, Solid Free. Fabr. 2016 Proc. 27th Annu. Int. Solid Free. Fabr. Symp. - An Addit. Manuf. Conf. SFF 2016. (2016) 2204–2216.

- [15] W.W. Wroe, J. Gladstone, T. Phillips, S. Fish, J. Beaman, A. McElroy, In-situ thermal image correlation with mechanical properties of nylon-12 in SLS, *Rapid Prototyp. J.* 22 (2016) 794–800. <https://doi.org/10.1108/RPJ-10-2015-0158>.
- [16] D. Drummer, K. Wudy, M. Drexler, Influence of energy input on degradation behavior of plastic components manufactured by selective laser melting, *Phys. Procedia.* 56 (2014) 176–183. <https://doi.org/10.1016/j.phpro.2014.08.160>.
- [17] C.L.A. Leung, S. Marussi, R.C. Atwood, M. Towrie, P.J. Withers, P.D. Lee, In situ X-ray imaging of defect and molten pool dynamics in laser additive manufacturing, *Nat. Commun.* 9 (2018) 1–9. <https://doi.org/10.1038/s41467-018-03734-7>.
- [18] M.R. Gardner, A. Lewis, J. Park, A.B. McElroy, A.D. Estrada, S. Fish, J.J. Beaman, T.E. Milner, In situ process monitoring in selective laser sintering using optical coherence tomography, *Opt. Eng.* 57 (2018) 1. <https://doi.org/10.1117/1.oe.57.4.041407>.
- [19] B. Zhang, J. Ziegert, F. Farahi, A. Davies, In situ surface topography of laser powder bed fusion using fringe projection, *Addit. Manuf.* 12 (2016) 100–107. <https://doi.org/10.1016/j.addma.2016.08.001>.